The Effect of the Antiscatter Grid on Full-Field Digital Mammography Phantom Images

Dev P. Chakraborty

Computer Analysis of Mammography Phantom Images (CAMPI) is a method for making quantitative measurements of image quality. This article reports on a recent application of this method to a prototype full-field digital mammography (FFDM) machine. Images of a modified ACR phantom were acquired on the General Electric Diagnostic Molybdenum Rhodium (GE-DMR) FFDM machine at a number of x-ray techniques, both with and without the scatter reduction grid. The techniques were chosen so that one had sets of grid and non-grid images with matched doses (200 mrads) and matched gray-scale values (1500). A third set was acquired at constant 26 kVp and varying mAs for both grid conditions. Analyses of the images yielded signal-to-noise-ratio (SNR), contrast and noise corresponding to each target object, and a non-uniformity measure. The results showed that under conditions of equal gray-scale value the grid images were markedly superior, albeit at higher doses than the non-grid images. Under constant dose conditions, the non-grid images were slightly superior in SNR (7%) but markedly less uniform (60%). Overall, the grid images had substantially greater contrast and superior image uniformity. These conclusions applied to the whole kVp range studied for the Mo-Mo target filter combination and 4 cm of breast equivalent material of average composition. These results suggest that use of the non-grid technique in digital mammography with the GE-DMR-FFDM unit, is presently not warranted. With improved uniformity correction procedure, this conclusion would change and one should be able to realize a 14% reduction in patient dose at the same SNR by using a non-grid technique.

KEY WORDS: digital mammography, breast imaging, technique optimization, antiscatter grid.

FULL-FIELD DIGITAL mammography is a promising new modality for breast imaging.[1] Several manufacturers are developing digital imaging devices and some are undergoing preclinical evaluation. Our institution is one of five hospitals that have prototype General Electric DMR full-field digital mammography (FFDM) machines installed. The FFDM machine consists of a standard DMR x-ray unit with a digital detector in place of the usual screen-film cassette. The detector consists of a CsI screen optically coupled to an amorphous silicon array. The latter has a two dimensional array of 100 μm × 100 μm pixels that can be read out under computer control using thin-film-transistor (TFT) technology. The machine has an additional capability of acquiring 50 μm images, but this was not used in this study. The detector field-of-view is nominally 8 in. × 10 in. images. The machine produces 1800 × 2304 × 16 bit images. Of the 16 bits, only 14 bits represent useful gray-scale data.

Computer Analysis of Mammography Phantom Images (CAMPI) is an image quality evaluation method that was introduced by us.[2,3] Although it is applicable to any uniform background phantom, all our past work has been with the American College of Radiology (ACR) mammography accreditation phantom.[4,5] Early applications of CAMPI were to analog screen-film mammography systems, but recent work has extended these measurements to digital mammography with small-field-of-view biopsy machines.[6,7] The method requires obtaining several *insert images* of the phantom wax insert, the extraction of regions-of-interest (ROIs) containing the target structures from these images, registering the ROIs corresponding to a given target to each other and averaging them. For each target type, the final averaged ROI (*template*) is used to calculate the image quality indices for the actual images to be evaluated (*test images*).

Unlike conventional radiography, which has undergone many decades of optimization, experience with full-field digital mammography is comparatively limited. The digital detectors have different physical characteristics from analog screen-film and optimal imaging parameters for digital mammography have yet to be established. Although many simulation studies and some measurements have been performed on general radiographic,[8] xero-radiographic,[9] conventional mammographic,[10-12] and digital-mammographic machines,[13-15] we know of no studies that actually measured the image quality of realistically shaped targets in phantom

From the Department of Radiology, University of Pennsylvania, Philadelphia, PA.

Partially supported by US Public Health Service's Office on Women's Health, Department of Health and Human Services, under contract number RFP 282-97-0077.

Address reprint requests to Dev P. Chakraborty, PhD, University of Pennsylvania, Department of Radiology, 3400 Spruce St, Philadelphia, PA 19104.

0897-1889/99/1201-0007$10.00/0

images. In our opinion, the CAMPI method is a natural approach for this type of measurement driven optimization.

Grids are ubiquitous in radiology, and their use, especially in higher kVp imaging of thick body parts (eg, an abdomen examination) is well accepted. Mammography is performed at lower kVp's and typically, the breast thickness is less than 6 cm thick. Accordingly, the rationale for the use of a grid in mammography is less clear-cut, especially with digital detectors. One argument advocated for a non-grid technique is that the superior contrast resolution of the digital images could be used to effect a dose reduction by performing digital mammography without a grid. In effect, the contrast lost by not using a grid could be recovered by proper windowing. We are aware that some institutions are contemplating using non-grid techniques for digital mammography. The purpose of this investigation was to determine which technique was superior, grid or non-grid, for a breast of average thickness and average composition for the GE-DMR FFDM machine.

METHODS

Acquiring Images

A special variable-thickness and variable composition phantom was constructed which included the insert plate obtained from an ACR phantom (serial number 505-067). The bottom face of the insert plate was positioned 3.3 cm above the base of the phantom, thereby matching the geometrical magnification in the ACR accreditation phantom. This phantom, shown schematically in Fig 1, allowed us to study 3 compositions, 50 to 50 (percentage glandular versus percentage fat equivalent), 30 to 70 and 70 to 30, respectively.

For each composition, we could vary the thickness from 2 cm to 8 cm in 1-cm steps. The breast equivalent material was obtained from CIRS (Computerized Image Reference Systems Inc; Norfolk, VA). For this study, we focused on the 50 to 50 composition and 4-cm thickness.

The DMR FFDM machine anode has two focal track *target* materials (Molybdenum, Mo, or Rhodium, Rh) and three filters (Mo, Rh, and Aluminum, Al). For this study, we selected the Mo-Mo target/filter combination. The insert images were obtained by imaging the wax insert only (no added material). The test images were of the phantom with 4 cm of 50 to 50 breast equivalent material added, which was positioned symmetrically under and above the insert. We use the convention described elsewhere of referring to the microcalcification groups,[3] in decreasing order of size, as M1, M2, M3, M4, and M5. Similarly, one has N1, N2, N3, N4 and N5 for the nodules and F1, F2, F3, F4, F5, and F6 for the fibers.

We started data acquisition by removing the grid and performing a "Detector Calibration" using the GE software available on the acquisition station. This involves imaging a 1 in thick acrylic phantom that covers the entire detector area. First, one

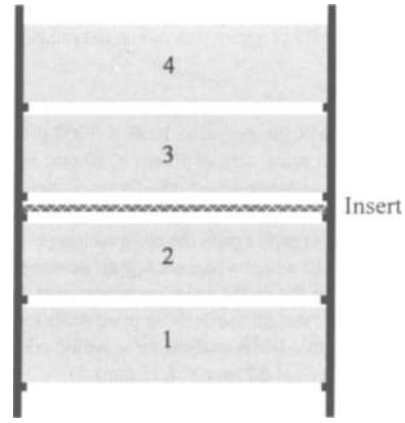

Fig 1. This is a schematic of the modified ACR phantom used in this study. Plates 1 through 4 are removable and determine the total thickness and composition of the phantom. The insert plate, obtained from an ACR phantom, was positioned so that the geometrical magnification matched that in the ACR phantom.

acquires two images at different mAs values to identify "bad pixels," ie, pixels whose mAs response is not linear. Second, one acquires four images at constant techniques to implement a "gain calibration," ie, to compensate for variations in gains and offsets of the amplifiers and other sources of non-uniformity. As a part of the calibration, the software saves certain files that are subsequently applied to newly acquired uncorrected images to correct them. The net effect is to achieve good flat-field uniformity for this phantom (to better than 1%). We refer to the above procedure as "calibration of the relevant non-grid files." Next, ten insert images were obtained under the non-grid condition at 22 kVp and 35 mAs. This was followed by the acquisition of three sets of test images, one at constant kVp (=26), the second at constant pixel value (CPV = 1500) and the third at constant mean glandular dose (=200 mrads). In the constant kVp condition the mAs was varied over the range 5 to 280. The mAs values needed for CPV were calculated from trial images by using the confirmed proportionality of the pixel value to mAs at fixed kVp (see below). The mAs needed for constant dose (CD) of 200 mrads were calculated from prior measurements of radiation exposure and half-value-layer as a function of kVp. A standard technique[16] and tabulated data[17,18] were used to calculate the Mean Glandular Dose (MGD). To interpolate between data points, a functional form (a second order polynomial in kVp and HVL) was least squares fitted to the tabulated MGD per Roentgen data. This allowed us to solve for any of the quantities MGD, kVp and mAs, given the other two. The accuracy of the fitting procedure was better than 3%. The DMR unit did not have continuously selectable mAs values. Therefore, we acquired images at two bracketing mAs values at each kVp for both CPV and CD sets. Linear interpolation was used to calculate each CAMPI measure from the two bracketing values. Following the non-grid image acquisition, the grid was replaced, the relevant grid FFDM files were calibrated as described previously, and the entire set of image acquisitions described above was repeated. The acquired images were transferred to the CAMPI workstation, archived on an optical disk and cropped

down to 1000 × 1000 regions encompassing the phantom. At this point, the CAMPI program was run on the images.

Analysis

The cropped DMR images were 1000 × 1000 pixels, which corresponded to an actual size of 10 cm × 10 cm, as the pixels were 100 μm. Our software was originally developed to analyze 2032 × 2032 images, with 50 μm pixels. The first step in the analysis was to digitally magnify the cropped images by a factor of 2 to 2000 × 2000 pixels, where each pixel now represents 50 μm. This allowed us to use the program with minimal modifications. For example, we still use 31 × 31 pixel ROIs for the speck regions. On the actual DMR images, these would correspond to 15.5 × 15.5 pixels (ie, 1.55 mm × 1.55 mm).

The CAMPI indices are defined in our previous publications.[3,6] If one plots along the x-axis the gray-scale values from the template, and along the y-axis gray-scale values from the test image, one obtains a quasi-linear plot. One performs least-squares linear regression to this data and determines the best-fit straight line. The COR (correlation) index is defined as the linear correlation coefficient between the x and y values after the template has been aligned with the test image data. Image alignment was performed by iteratively maximizing the correlation coefficient. The slope of the regression straight line is called the SIG (signal) measure. The NOI (noise) index is defined as the fitting noise of the regression line. The PV (pixel value) index was defined as the ordinate value corresponding to an abscissa of 1500 (arbitrarily chosen). The speck SNR is defined as the ratio of two cross-correlation values, the *signal* and the *noise* respectively. Each cross correlation value is measured with an aperture having the same size and shape as the target object. The *noise* is defined as the standard deviation of the cross correlation values measured at background (noise) locations, and should not be confused with the microcalcification fitting noise measure NOI defined earlier. The *signal* is defined as the incremental cross correlation value measured at the speck (signal) location. It should not be confused with the SIG measure defined earlier. Formally, SNR equals signal/noise.

In an earlier paper[19] we showed that both COR and SNR are strongly correlated (Kendall correlation coefficient >90%) with human observers' subjective impressions of image quality of the target objects. Because of limited background area availability for noise sampling, the SNR measure is not useful for the larger target objects (eg, the fibers and nodules) whereas the COR measure is applicable to any size object. We have shown[7] that the COR measure can be transformed to a signal-to-noise-ratio like quantity, called SNR (COR), which is defined by

$$\mathrm{SNR(COR)} = \frac{\mathrm{COR}}{\sqrt{1 - \mathrm{COR}^2}}. \qquad (1)$$

If the correlation between the test image region of interest (ROI) and the template ROI is perfect, one has COR = 1 and SNR (COR) = ∞. Likewise zero correlation, COR = 0, leads to SNR (COR) = 0. *In this work, we used SNR (COR) instead of SNR.* For brevity, SNR (COR) will henceforth be abbreviated to SNR.

In addition to the usual CAMPI indices, we calculated a non-uniformity index in the following manner. As part of CAMPI analysis, the operator identifies up to four rectangular regions in the image, none of which includes any target objects. We sampled these regions using 31 by 31 pixel samples. For each sample, we calculated the average pixel value. About 600 non-overlapping samples were obtained from the rectangular regions. The coefficient of variance of the values was defined to be a non-uniformity index (NU). The CAMPI alignment algorithm allowed us to calculate the non-uniformity index using *exactly* the same rectangular regions on all images.

RESULTS

Presented in Figs 2, 3, and 4 are plots of SNR vs. kVp, under CPV conditions, for the grid and nongrid images. In each case, the measures have been averaged over all target groups. This was done (a) to obtain a more stable number to report and (b) to make the results more compact and easier to present. For example, the microcalcification plot (Fig 2) is an average over M1, M2 and M3. Similarly, the fiber plot (Fig 3) is an average over F1, F2, F3, and F4, and the nodule plot (Fig 4) is an average over N1, N2, N3, and N4. Note that in each case the grid plot is above the corresponding non-grid plot. In other words, if the image receptor is exposed to the same pixel value (this will lead to about a factor of 2-3 higher patient dose under the grid condition), it is advantageous to use the grid. Also evident from these figures is the decreasing behavior of SNR as kVp increases under constant pixel value conditions. This is consistent with the observed behavior for other digital mammography machines that we have studied using the CAMPI method.[6] It is also consistent with the results of other work (our CPV and constant dose data should be compared to Figs 6 and 7, respectively, in ref. 20). Figure 5 shows the variation of the non-

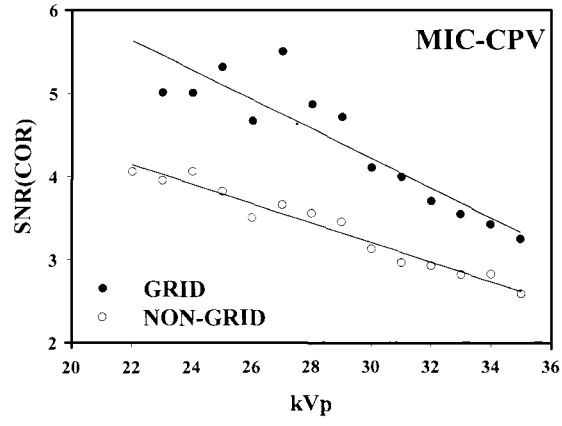

Fig 2. This shows a plot of microcalcification SNR vs. kVp, averaged over M1, M2 and M3, under constant pixel value (CPV) condition for the grid and non-grid images. Note that under this condition the grid images, which are produced with a higher radiation dose, are superior to the non-grid images.

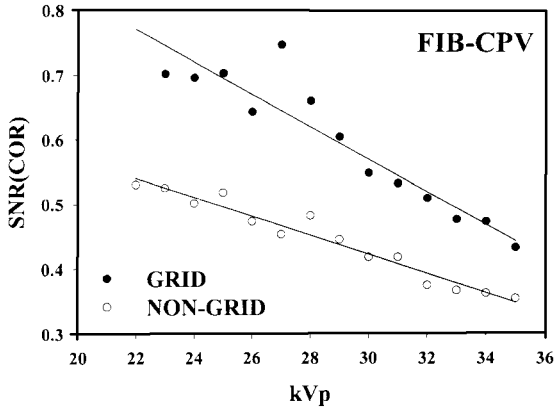

Fig 3. This shows a plot of fiber SNR vs. kVp, averaged over F1, F2, F3, and F4, under constant pixel value (CPV) condition for the grid and non-grid images. The grid images are seen to be superior to the non-grid images.

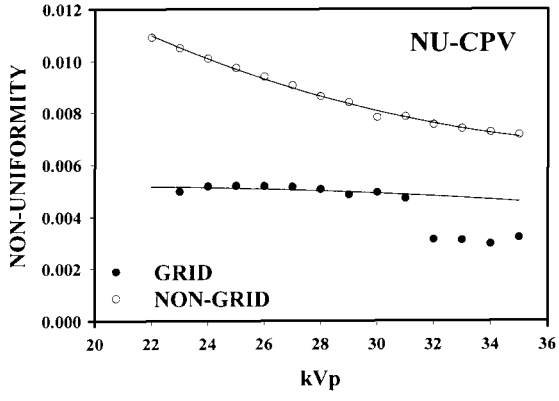

Fig 5. This is a plot of the non-uniformity measure (NU) vs. kVp for the CPV data set under grid and non-grid conditions. Note the small values of the non-uniformity index (<1.4%) and that the grid images have better uniformity than the non-grid. The discontinuity is explained in the text.

uniformity index of the CPV set as a function of kVp for the grid and non-grid conditions. Note the substantially larger non-uniformity of the non-grid images, which is about 60% more at 26 kVp, and the difference decreases as kVp increases. The discontinuity in the grid data at 31 kVp was caused by an interrupted acquisition resulting from a software problem. When acquisition was resumed a few days later, the machine had to be recalibrated and the non-uniformity was smaller. The data was not reacquired, as the effect on the SNR was minimal.

The results of analysis of the constant dose set are shown in Figs 6, 7, and 8, which are plots of SNR versus kVp for the microcalcifications, fibers, and nodules, respectively. Note that in each case the non-grid curve is above the grid curve, although the difference is small (about 7% in each case). In other words, if the dose is held constant (this will result in higher pixel values for the non-grid images) there may be a small advantage in signal-to-noise-ratio to *not* using the grid. Note that each curve shows a maximum at about 26 kVp. This means that 26 kVp is near optimal in terms of providing the maximum signal-to-noise ratio for a specified dose. A slightly higher kVp (27-28) may be preferable, in practice, to minimize motion blur. We emphasize that these results apply only to a 4 cm 50 to 50 composition breast. There has been, of course, a lot of work in the past on technique optimization for screen-film mammography.[11,12] Our

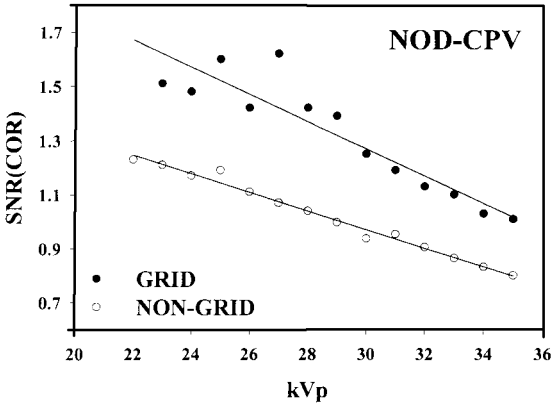

Fig 4. This shows a plot of nodule SNR vs. kVp, averaged over N1, N2, N3 and N4, under constant pixel value (CPV) condition for the grid and non-grid images. The grid images are seen to be superior to the non-grid images.

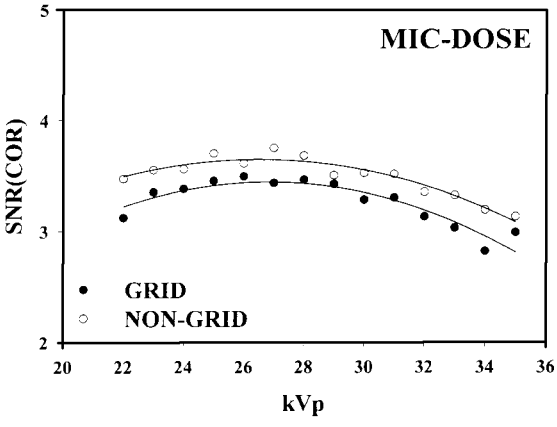

Fig 6. This shows a plot of microcalcification SNR vs. kVp, averaged over M1, M2 and M3, under constant dose condition for the grid and non-grid images. Note the slight superiority of the non-grid set.

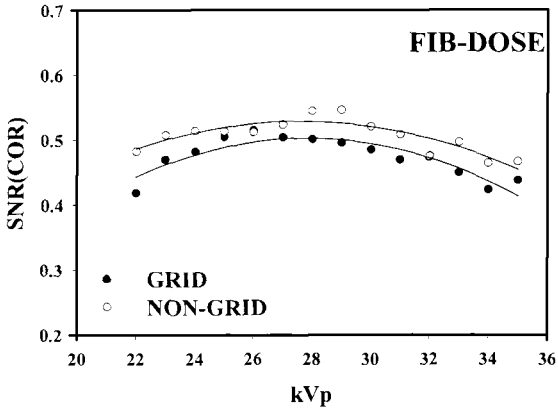

Fig 7. This shows a plot of fiber SNR vs. kVp, averaged over F1, F2, F3 and F4, under constant dose condition for the grid and non-grid images. Note the slight superiority of the non-grid set.

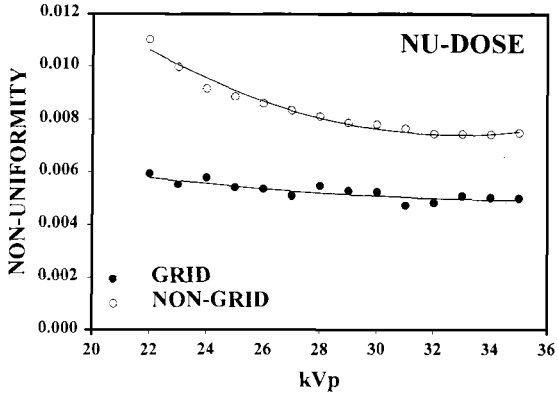

Fig 9. This shows the variation of the non-uniformity index of the constant dose set as a function of kVp for the grid and non-grid conditions. Note the substantially larger non-uniformity of the non-grid images, which is about 60% more at 26 kVp, and the difference decreases as kVp increases.

results should be compared to Fig 15 in reference 12, which shows an optimal kVp of about 27 for a 4-cm breast thickness. Figure 9 shows the variation of the non-uniformity index of the constant dose set as a function of kVp for the grid and non-grid conditions. Note, again, the substantially larger non-uniformity of the non-grid images, which is about 60% more at 26 kVp, and the difference decreases as kVp increases. As in Fig 5, the grid curve is seen to be relatively flat as a function of kVp.

Presented in Figs 10, 11, 12, and 13 are images of the phantom obtained under different conditions. Figure 10 is an insert image, ie, an image obtained with no scattering material in the beam, at 22 kVp and 35 mAs. Note the excellent visibility of the target objects in this image: *all* target objects were

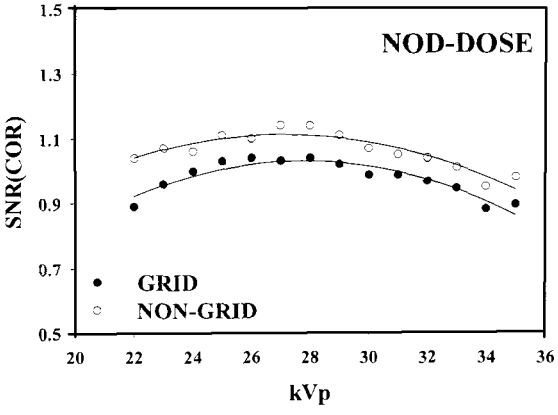

Fig 8. This shows a plot of nodule SNR vs. kVp, averaged over N1, N2, N3 and N4, under constant dose condition for the grid and non-grid images. Note the slight superiority of the non-grid set.

visible on the monitor under proper display conditions. Ten images like this were used to construct the CAMPI templates. Figure 11 is a grid image obtained at 26 kVp and 225 mAs. Figure 12 is a grid image obtained at 26 kVp and 100 mAs. Finally, Fig 13 is a non-grid image obtained at 26 kVp and 100 mAs. Figures 11 and 13 represent a CPV set as each image had a pixel value of 1500. The difference in image quality between these (with the grid being superior) is obvious and consistent with the SNR and non-uniformity results in Figs 2, 3, 4, and 5. Note that this superiority is obtained at a factor of 2.25 higher dose to the patient. Figures 12 and 13 represent a constant dose set as they have identical kVp and mAs values. The grid image is seen to be noisier but has better uniformity than the non-grid image. The poorer uniformity of the non-grid images degrades the visibility of the first four fibers in the printed copy, but this can be overcome with local windowing on the monitor. Visual interpretation of these images yielded target counts of 4.0/5.0/4.0 (corresponding to microcalcifications, fibers and nodules) and 4.0/5.5/4.5, for the grid and non-grid images, respectively. These confirm the CAMPI results that an increase in target visibility can be obtained under constant dose conditions using the non-grid technique. These interpretations were performed on a video monitor (Image Systems 24 in portrait monitors, 1200 × 1600) by the author. Note that all DMR images in this paper are rotated 90° counter-clockwise from the normal presentation on the DMR acquisition station. The anode cathode axis

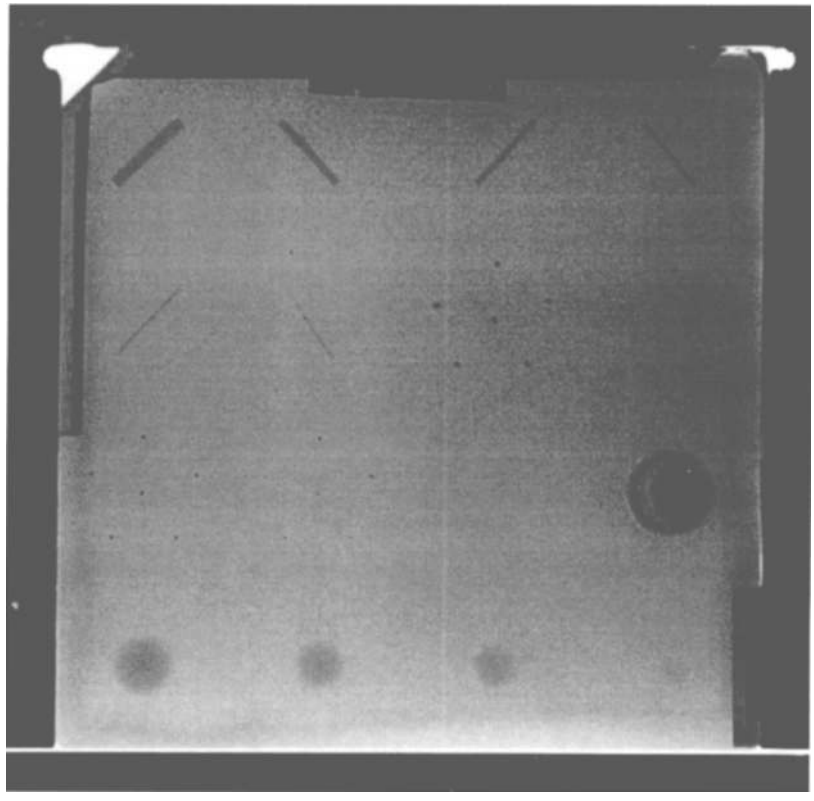

Fig 10. This is an insert image, ie, an image obtained with no scattering material in the beam, at 22 kVp and 35 mAs. Note the excellent visibility of the target objects in this image: all target objects were visible on the monitor under proper display conditions.

NON-GRID, INSERT

runs vertically in the figures (N2, N3, N4, and N5 are at the chest wall end of the image receptor). The pixel overflow artifacts in the images are all printer-generated and are not visible when displayed on the monitor. The display contrast of the image shown in Fig 13 was larger than that of the other three—this tended to make the non-uniformity more visible.

The relative contrast (cnt = SIG/PV), the relative noise (noi = NOI/PV) and the contrast-to-noise ratio (cnr = cnt/noi), are summarized in Table 1 for the three images shown in Figs 11, 12, and 13. Note that the relative contrast in the non-grid images is significantly smaller than in the grid images (about 70% of the latter) but the relative noise is also smaller. This leads to a small increase in the contrast-to-noise ratio of the non-grid images (eg, Fig 13) over the corresponding equal-dose grid images (eg, Fig 12). Note that cnt, noi and cnr, respectively, are not the same as SIG, NOI and SNR.

Figures 14, 15, and 16 are the SNR results for the 26 kVp set of images. These follow an approximate square-root dependence on mAs.[7] Note that, except for the fibers, the non-grid curves lie above the grid curves. This means that the slight superiority (in SNR measure) of the non-grid images at 26 kVp is true for a range of dose values, not just 200 mrads. Finally, Fig 17 shows the non-uniformity index as a function of mAs at 26 kVp. Note that the non-uniformity index is constant as a function of mAs. This follows from the close linearity of the digital detector. For example, a plot of PV versus mAs (not shown) at constant kVp is quite linear (correlation coefficient >0.999). The NU measure is the coefficient of variance of the averaged pixel values. Doubling the mAs should double both the standard deviation and the average pixel value. Their ratio, the NU measure, is unchanged.

DISCUSSION

For digital imaging of a 4 cm thick breast of average composition, several conclusions can be made from this work. They are (1) image quality at

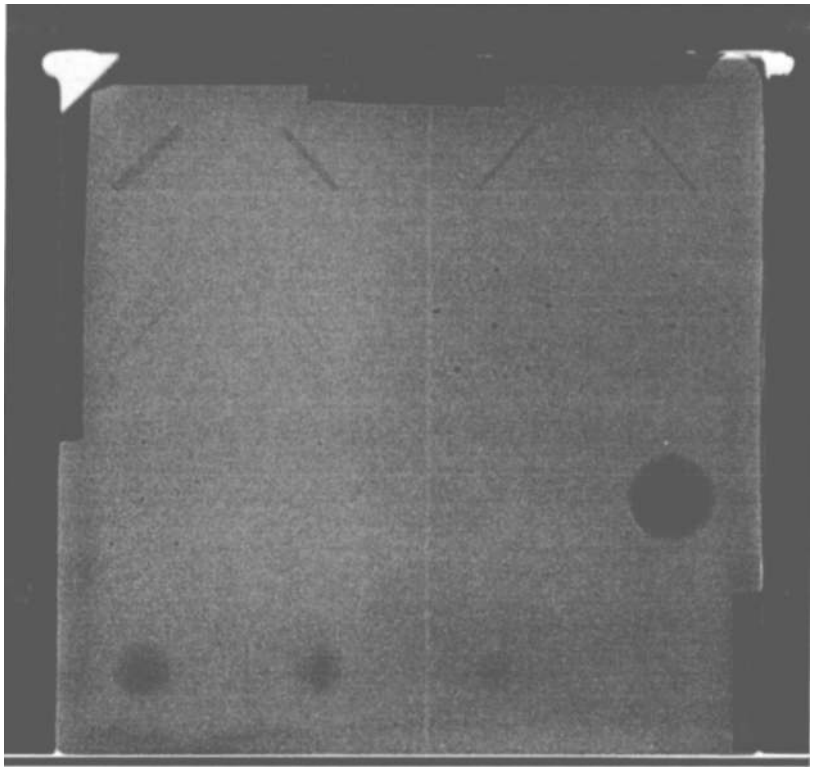

GRID, 26 kVp, 225 mAs

Fig 11. An image of the ACR phantom obtained at 26 kVp and 225 mAs with grid. Note the decreased visibility relative to Fig 10, which is due to the additional scattering material and the higher kVp.

constant pixel value degrades with increasing kVp; (2) image quality at constant dose shows a broad maximum near 26 kVp; (3) image quality increases with mAs at constant kVp. (4) Regarding the effect of the two grid conditions, under conditions of equal pixel value, the grid images are substantially superior, albeit at significantly higher doses (a factor of 2.2 at 26 kVp). (5) Under conditions of equal-dose, the grid images are inferior in SNR (7%) but superior in uniformity (60%) to the non-grid images.

The grid images also have more contrast and more noise than the non-grid images. As is well known, the scatter suppression effect of the grid increases the contrast by the Contrast Improvement Factor.[21] The increased noise is because the grid absorbs some of the radiation (Bucky Factor) which leads to increased quantum mottle. With the low contrast and noise levels achieved for the non-grid images, residual (ie, non-x-ray related) non-uniformity in the image can assume greater importance. This may explain the different texture of the noise in the non-grid images (to the author it had a "blotchy" appearance) from that in the grid images. In other words, the small SNR advantage of the non-grid condition may not lead to a net improvement in image quality if it is overshadowed by poorer uniformity and contrast. Unlike the flat-field calibration phantom, the phantom used in this work did not cover the entire field-of-view, as it resembled a normal sized breast. We suspect that the differences between the scatter fields associated with the calibration and the test phantoms accounts for the increased non-uniformity of the non-grid images. The explanation for why this mainly affects the non-grid images is that the presence of the grid removes the scatter, which makes variations in the scatter fields less important. We observed that the uniformity of the non-grid images was sensitively dependent on the position of the phantom. Figure 13 is an example of a non-grid image that exhibited the *least* non-uniformity. This was obtained by positioning the scatter blocks symmetrically (in the horizontal plane) relative to the insert. Additional non-uniformity is contributed by the non-flat nature of the phantom insert, whose thick-

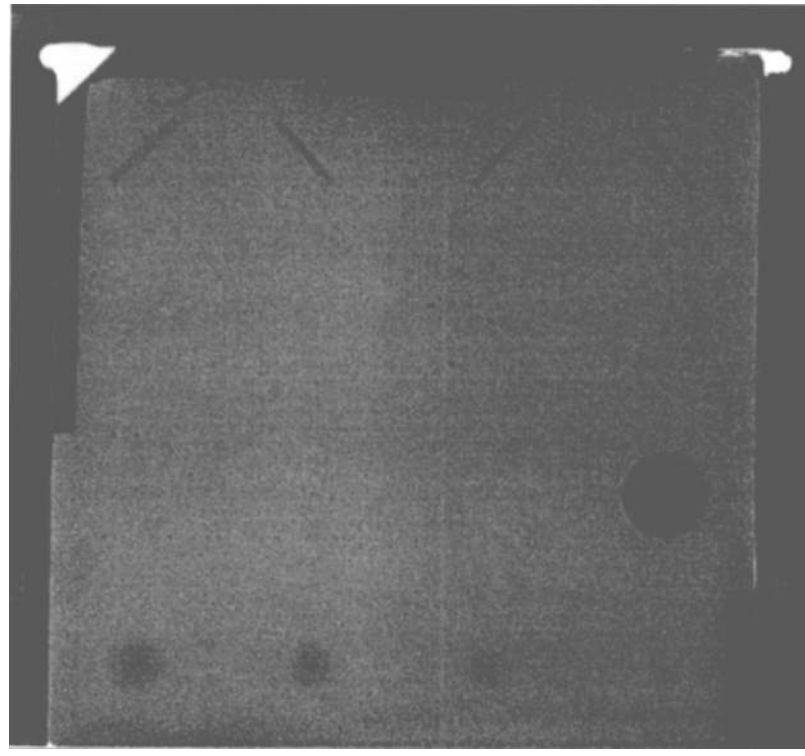

Fig 12. An image of the ACR phantom obtained at 26 kVp and 100 mAs with grid. Note the decreased visibility relative to Fig 11, due to the smaller mAs value. Compare this to the non-grid image shown in Fig 13.

ness decreases near the edges. The overall non-uniformity affects the fibers mainly, and this is likely the reason for the inconsistency between the 100 mAs fiber results in Fig 15 and the 26 kVp result in Fig 7. The two runs, from which these data are derived, were actually different physical runs and phantom positioning and/or calibration files were probably not identical. In prior acquisitions, we observed severe non-uniformity in the non-grid images, which were visually inferior to the corresponding equal-dose grid images. With improved uniformity correction, one could realize a dose reduction of 14% (since the SNR is proportional to the square root of the dose) by using a non-grid technique. The improvement would have to take into account the scatter field of the object being imaged and methods are described in the literature.[22,23]

The DQE of the grid and non-grid modes can be estimated from available data as follows. The DQE is the product of the scatter degradation factor (SDF) and the primary transmission (T_p) of the device.[24] Here "device" can be taken to mean "grid" or "non-grid." Therefore, $DQE = T_p\,SDF = T_p\,[1/(1 + s/p)]$, where s/p is the scatter to primary ratio. Taking data from Barnes and Frey[25] for a particular (Transworld) grid, a 4 cm breast and 30 kVp, s/p = 0.19 and T_p = 0.69. This leads to DQE_{grid} = 0.580. For no grid, s/p = 0.617 and T_p = 1.00 so $DQE_{non\text{-}grid}$ = 0.618. The DQE ratio (non-grid to grid) is 1.066, whose square root (1.03) should be compared to the SNR ratio (1.07) yielded by our measurements. The agreement is rather good considering the uncertainties in all the measurements. Note that s/p is sensitively dependent on the phantom construction and the type of grid used. Both of these differed between our measurements and the measurements reported elsewhere.[25]

The SNR indices were relatively insensitive to image non-uniformity. For example, the microcalcification SNR measure is calculated over a 1.5 mm × 1.5 mm region for the DMR images. Non-uniformity over this small area is consequently negligible. The nodule and fiber measures actually involve subtracting a fitted background from the local region. The algorithm resembles an idealized

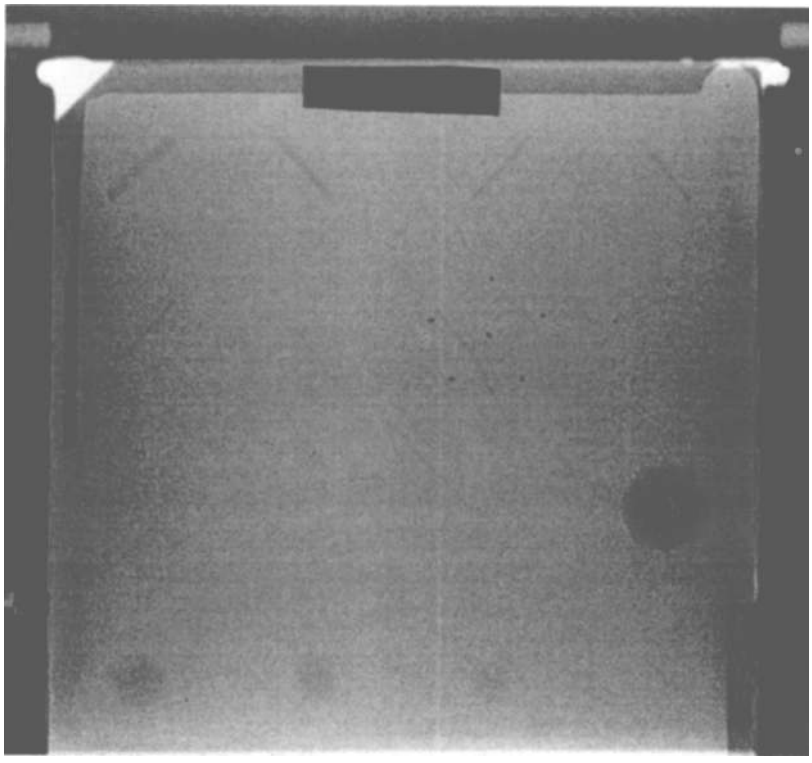

Fig 13. An image of the ACR phantom obtained at 26 kVp and 100 mAs without grid. Note the non-uniformity in the image. On the monitor, the target visibility is slightly superior to that in Fig 12.

NON-GRID, 26 kVp, 100 mAs

Table 1. CAMPI Measurements

Figure	mAs	Condition	Target Type	cnt	noi	cnr = cnt/noi
11	225	Grid	MICRO	1.71E-04	6.45E-03	2.65E-02
12	100	Grid	MICRO	1.73E-04	9.16E-03	1.88E-02
13	100	Non-Grid	MICRO	1.22E-04	6.39E-03	1.91E-02
11	225	Grid	FIBER	2.72E-04	5.15E-01	1.50E-02
12	100	Grid	FIBER	2.74E-04	5.05E-01	9.26E-03
13	100	Non-Grid	FIBER	1.49E-04	5.09E-01	9.80E-03
11	225	Grid	NOD	2.31E-04	5.04E-01	1.31E-02
12	100	Grid	NOD	2.41E-04	5.03E-01	8.85E-03
13	100	Non-Grid	NOD	1.62E-04	4.87E-01	8.91E-03

NOTE. This is a summary of CAMPI measurements for the three 26 kVp images displayed in Figs 11-13. Listed are the x-ray techniques, the target type, the relative contrast (cnt = SIG/PV), the relative noise (noi = NOI/PV) and the contrast-to-noise-ratio (cnr = cnt/noi). Note the following general features. (1) The relative contrast is the same for the two grid images and larger than that of the non-grid image. (2) The relative noise is least for the non-grid images. (3) The cnr is highest for the grid image at 225 mAs. (4) The cnr of the non-grid image is greater than that of the grid image at the same dose.

observer who is capable of compensating the images for predicable local non-uniformity. Since it impacts on the quality of the displayed image, it is clear that the non-uniformity measure is an important new quantity that should be evaluated along with the other measures in all future CAMPI work.

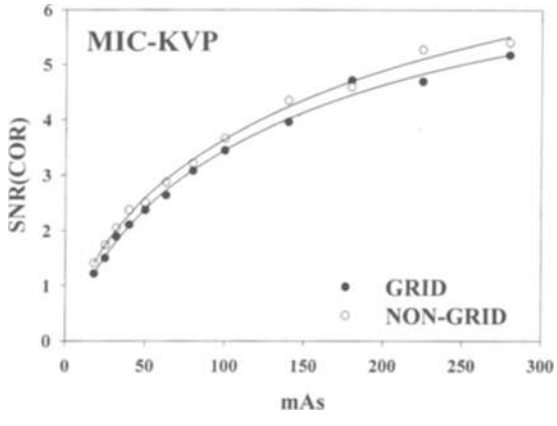

Fig 14. This compares the microcalcification SNR data obtained at 26 kVp vs. mAs under grid and non-grid conditions. Note the slight superiority of the non-grid images.

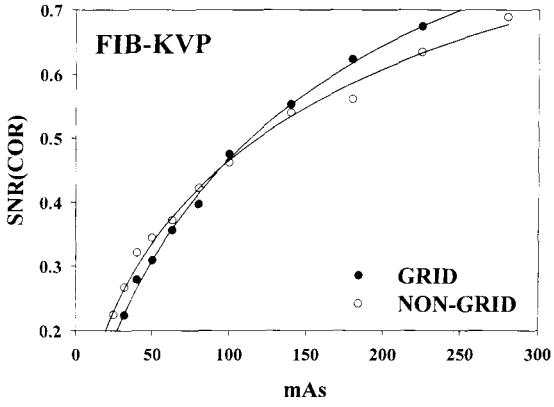

Fig 15. This compares the fiber SNR data obtained at 26 kVp vs. mAs under grid and non-grid conditions.

A figure-of-merit defined by the quotient of SNR and the square root of the dose is often used to normalize for the dose. Implicit in this definition is the assumption that the signal-to-noise-ratio is proportional to the square root of the dose (ie, the machine is quantum limited). In our case, this was not the case as the signal-to-noise-ratio had a more complex dependence[7] on mAs (or dose). The dependence found in earlier studies, and confirmed in the present work, was

$$\mathrm{SNR(COR)} = \frac{\mathrm{D} \cdot \mathrm{mAs}}{\sqrt{1 + \mathrm{E} \cdot \mathrm{mAs} + \mathrm{F(mAs)^2}}}. \quad (2)$$

Here D, E and F are mAs-independent constants, which are expected to depend on kVp, HVL, machine and phantom characteristics. Because of the more complex dependence of SNR on mAs (or dose), it is strictly not justifiable to use the SNR/sqrt (dose) normalization, as is usually assumed in

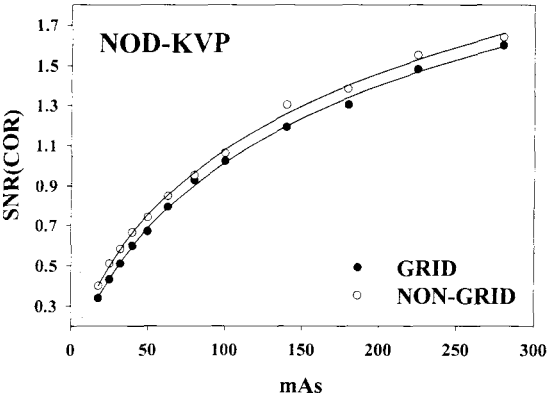

Fig 16. This compares the nodule SNR data obtained at 26 kVp vs. mAs under grid and non-grid conditions.

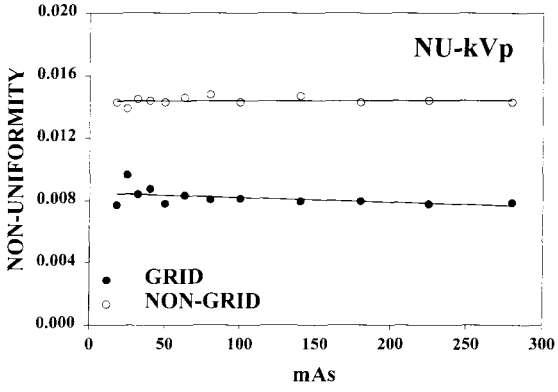

Fig 17. This is a plot of non-uniformity index (NU) vs. mAs for grid and non-grid images obtained at constant kVp (=26). Note that (1) the non-uniformity index is constant and (2) that the non-grid images have greater non-uniformity. The constancy follows from the linearity of the detector; see text.

theoretical studies of digital systems. Values of D, E and F for the non-grid data shown in Fig 14 were 0.0934, 0.0497, and 0.0001, respectively.

Examination of the plots in Figs 2, 3, and 4 shows that there was significant, correlated variation of the SNR values below 28 kVp for the grid images. It appears that this was restricted to this particular acquisition, as the other figures do not show as much variation. The correlation of the measures corresponding to the different target objects has been commented on before.[3] One source of variability is machine fluctuations: even if the technique factors are set identically, there could be differences in both the quantity and the quality of the radiation produced. There could also be mechanical effects associated with starting and stopping the grid. Another factor could be the CAMPI algorithm itself. Differences in alignment accuracy could produce correlated changes in CAMPI measures for all the targets (for example, better than average alignment accuracy would yield higher than normal values of the measures for all the target objects). Finally, one expects the measures to be intrinsically correlated as they are measured on the *same* image. These sources are all expected to produce correlated changes in the measures and separating the different effects is a challenging problem that we have not yet solved.

In the context of Quality Control (QC), the CAMPI method has several advantages over the usually performed visual analysis of phantom images. It eliminates interreader variability, since others can use the algorithm as a single, standard-

ized, numerical "reader." Intrareader variability (that observed when CAMPI is applied to the same digital image file) is very small (coefficient of variance CV $<10^{-4}$). When CAMPI is applied to the 10 insert images obtained under identical x-ray technique conditions, the resulting SNR values typically have CV ~5%. Because this is much larger than the intrareader term, we attribute it to case-sampling variability, ie, to true image-to-image fluctuations obtained when images are obtained under identical technique conditions. Note that above error estimate of 5% is comparable to that observed in the present study, if one excludes the few anomalous data points mentioned earlier.

To summarize our results, use of the non-grid technique is not recommended for a 4-cm breast of average composition for the DMR FFDM machine studied. With improved uniformity correction, this conclusion could change. If the uniformity of the non-grid images were as good as that of the grid images, it would be possible to realize a 14% reduction in patient-dose using a non-grid technique. This study was restricted to the effect of the anti-scatter grid. As part of an overall optimization of the DMR digital machine, we have plans to extend the present measurements to optimize other machine parameters.

ACKNOWLEDGMENT

The author is grateful to Heidi Leister for assistance with the data acquisition, analysis and manuscript editing. The author also is grateful to an anonymous reviewer who provided the DQE estimates.

REFERENCES

1. Feig SA, Yaffe MJ: Current Status of Digital Mammography. Semin Ultrasound, CT and MR 17:424-43, 1996

2. Eckert MP, Chakraborty DP: Quantitative Analysis of Phantom Images in Mammography. Proc SPIE 2167:887-899, 1994

3. Chakraborty DP, Eckert MP: Quantitative versus Subjective Evaluation of Mammography Phantom Images. Med Phys 22:133-143, 1995

4. Chakraborty DP: Physical measures of image quality in mammography. Proc SPIE 2708:179-193, 1996

5. Chakraborty DP: Computer analysis of mammography phantom images (CAMPI). Proc SPIE 3032:292-299, 1997

6. Chakraborty DP: Computer Analysis of Mammography Phantom Images (CAMPI): An Application to the Measurement of Microcalcification Image Quality of Directly Acquired Digital Images. Med Phys 24:1269-1277, 1997

7. Chakraborty DP, Fatouros PP: An Application of CAMPI Methodology: Comparison of two Digital Biopsy Machines. Proc SPIE 3336:618-628, 1998

8. Motz JW, Danos M: Image information content and patient exposure. Med Phys 5:8-22, 1978

9. Muntz EP, Welkowsky, Kaegl E, et al: Optimization of electrostatic imaging systems for minimum patient dose or minimum exposure in mammography. Radiology 127:517-523, 1978

10. Muntz EP, Jafroudi H, Jennings R, et al: An approach to specifying a minimum dose system for mammography using multiparameter optimization techniques. Med Phys 12:5-12, 1985

11. Muntz EP: Analysis of the significance of scattered radiation in reduced dose mammography, including magnification effects, scatter suppression, and focal spot and detector blurring. Med Phys 6:110-117, 1979

12. Jennings RJ, Quinn PW, Gagne RM, et al: Evaluation of x-ray sources for mammography. SPIE 1896:259-268, 1993

13. Williams MB, Fajardo LL: Digital Mammography: Performance considerations and current detector designs. Acad Radiol 3:429-37, 1996

14. Liu H, Fajardo LL, Barrett JR, et al: Contrast-detail detectability analysis: Comparison of a digital spot mammography system and an analog screen-film mammography system. Acad Radiol 4:197-203, 1997

15. Court LE, Speller R: A multiparameter optimization of digital mammography. Phys Med Biol 40:1841-1861, 1995

16. Hendrick RE, Bassett L, Botsco MA, et al: Mammography Quality Control Manual. American Cancer Society, American College of Radiology, 1994 (revised ed.)

17. Wu X, Barnes GT, Tucker DM: Spectral Dependence of Glandular Tissue Dose in Screen-Film Mammography. Radiology 179:143-148, 1991

18. Gingold EL, Wu X, Barnes GT: Contrast and Dose with Mo-Mo, Mo-Rh and Rh-Rh Target-Filter Combinations in Mammography. Radiology 195:639-644, 1995

19. Chakraborty DP: Comparison of computer analysis of mammography phantom images (CAMPI) with perceived image quality of phantom targets in the ACR phantom. Proc SPIE 3036:160-167, 1997

20. Fahrig R, Yaffe MJ: A model for optimization of spectral shape in digital mammography. Med Phys 21:1463-1471, 1994

21. Bushberg JT, Seibert A, Leidholdt EM, et al: The Essential Physics of Medical Imaging. Baltimore, MD, Williams and Wilkins, 1994

22. Seibert J, Boone JM: X-ray scatter removal by deconvolution. Med Phys 15:567-575, 1988

23. Molloi SY, Mistretta C: Scatter-glare corrections in quantitative dual-energy fluoroscopy. Med Phys 15:289-297, 1988

24. Wagner RW, Barnes GT, Askins BS: Effect of reduced scatter on radiographic information content and patient exposure: A quantitative demonstration. Med Phys 7:13-18, 1980

25. Barnes GT, Frey GD: Screen Film Mammography: Imaging Considerations and Medical Physics Responsibilities. Medical Physics Publishing, Madison, Wisconsin, 1991, pp 115-134